THE MICROBUNCHING INSTABILITY
AND LCLS-II LATTICE DESIGN

M. Venturini*

Lawrence Berkeley National Lab, Berkeley, CA 94720 USA

Abstract

The microbunching instability is a pervasive occurrence when high-brightness electron beams are accelerated and transported through dispersive sections, like bunch-compression chicanes or distributions beamlines. If left uncontrolled, the instability can degrade the beam brightness and compromise the FEL performance. This paper contains a discussion of how consideration of the microbunching instability is informing the LCLS-II design and determining the specifications for the laser heater and transport lines. We review some of the expected and not so-expected phenomena that we have encountered while carrying out high-resolution macroparticle simulations of the instability and the analytical models developed to interpret the numerical results.

INTRODUCTION

LCLS-II is a 4th-generation high-rep rate FEL light source soon to enter the construction phase at SLAC [1, 2]. The 4 GeV super-conducting Linac will occupy the first third of the existing SLAC Linac tunnel; a long (~ 2 km) transport line will bypass the remaining sections of the normal-conducting machine and deliver the beam to the existing undulator hall, with a fast kicker distributing the beam between the hard (HXR) and soft (SXR) x-ray FEL undulators. The baseline design (100 pC bunches with $I_f \simeq 800$ A or higher peak current at the FELs and $I_{gun} \simeq 3$ A at the gun) calls for two-stage magnetic-compression at 250 and 1600 MeV beam energy in addition to significant velocity-bunching or 'ballistic' compression in the injector before the beam becomes ultra-relativistic. Use of a third magnetic chicane placed immediately before the spreader at full 4 GeV beam energy is under consideration but will not be discussed here. For a summary of relevant machine parameters, see Table 1.

As in all 4th-generation light sources the microbunching instability is expected to be significant. The instability can be seeded by shot noise or other noise sources at the injector photo-cathode and develops through a combination of collective effects (primarily space-charge) and transport/compression along dispersive sections. The main adverse effect is the generation of uncorrelated or micro-correlated energy-spread growth. The instability can result into loss of radiated power and/or degradation of the radiation spectral properties, with tolerance to the instability depending on the mode of FEL operation (SASE, self-seeding, external seeding).

There are two aspects relevant to the instability that are specific to LCLS-II: the presence of long transport lines between the Linac and the undulators and reliance on velocity bunching for compression. Both have potentially aggravating effects. While in low rep-rate LCLS-class injectors, which are usually operated without velocity bunching, plasma oscillations at low energy tend to have a generally smoothing effect on perturbations to the charge density [3], the effect can be reduced or reversed in the presence of velocity bunching compression [4, 5]. This is most relevant for the instability seeded by non-uniformity in the photo-gun laser profile. Here we will not address this issue, focusing instead on consideration of microbunching seeded by shot noise, for which it is appropriate to model the development of the instability starting from the exit of the injector. In our study we use a combination of analytical and numerical methods to characterize the main drivers of the instability and related phenomena, and identify strategies for machine-design optimization. Topics of interest discussed here include the anomalous heating induced by the laser heater, the development of the instability through the magnetic compressors, and its further amplification through the transport lines downstream of the Linac. Our macroparticle simulations, carried out with the code IMPACT [6], are based on idealized models of the beam distribution (*e.g.* temporal flat-top, 6D water-bag) having the nominal characteristics (emittance, peak current) of the baseline beam at the exit of the injector and always employ the same number of macroparticles as the number of electrons to minimize spurious effects. Results from start-to-end simulations starting from the photo-cathode and including modelling of the radiation output are reported elsewhere [7, 8].

Table 1: LCLS-II Baseline Settings

Charge/bunch	100 pC
Peak current at exit of injector, I_{inj}	14 A
Peak current at FEL, I_f	800 A
Transverse normalized rms emittance, ε_n	0.3 μm
Beam energy at exit of injector, E_{inj}	100 MeV
Beam energy at BC1, E_{bc1}	250 MeV
Beam energy at BC2, E_{bc2}	1.6 GeV
Beam energy at FEL, E_f	4 GeV
BC1 R_{56}, R_{56}^{bc1}	-55 mm
BC2 R_{56}, R_{56}^{bc2}	-38 mm
BC1 compression factor, C_{bc1}	~ 6
BC2 compression factor, C_{bc2}	~ 10

---
* mventurini@lbl.gov
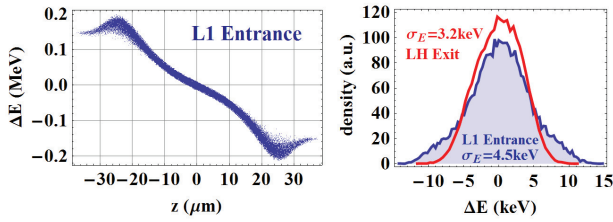
Figure 1: Longitudinal phase-space (left) of bunchlet at entrance of the first section of the Linac (L1) and energy density in the core (right, blue curve). For comparison, the red curve on the right figure is the energy density at exit of the LH chicane: the difference between the two is the result of trickle heating; σ_{E0} = 2 keV.

Figure 2: Energy spread at the entrance of L1 (two choices of laser wavelengths) showing evidence of the 'trickle' heating effect; σ_{E0} = 0.1 keV. The dashed line is the nominal heating in the absence of collective effects.

ANOMALOUS HEATING

'Trickle' Heating

The Laser Heater (LH) is the established method to control the microbunching instability, exploiting the microbunching sensitivity to energy-spread induced mixing. In LCLS-II the LH is located at the exit of the injector at about 100 MeV beam energy; it consists of a 0.54 m undulator placed in the middle of a weak 4-dipole chicane and a λ_L = 1030 nm laser system. Concerns about the 'trickle' heating effect, discovered during LCLS commissioning [9], motivated the close analysis reported here. Trickle heating is an echo-like phenomenon, in which the E/z micro-correlations generated by the laser/electrons interaction in a finite-dispersion region induce x/y correlations on the same micro-scale downstream of the LH (while the E/z micro-correlations are eventually washed out by the finite transverse emittance). The x/y correlations appear at relatively well localized points along the lattice separated by π phase advance in the horizontal betatron motion. The associated longitudinal space-charge forces modify the electron energy resulting into anomalous heating, which is undesirable, as it may compromise accurate control of the heater operation. To speed up the numerical calculations without sacrificing accuracy, we simulate a flat-top bunchlet meant to model a short section of the bunch core (but long enough to span many laser wavelengths).

We track the bunchlet with initial gaussian energy density and σ_{E0} slice rms energy spread, starting from the exit of the injector, a few meters upstream of the LH chicane; σ_{E0} from high brightness injectors is not known very well but is expect to be on the order of 1-2 keV, including IBS effects: in our simulations we exercised a range of values, down to 0.1 keV. The action of the laser on the beam is modeled as a point-like interaction inducing a sinusoidal energy modulation and occurring in the middle of the physical undulator. The electron dynamics through the undulator itself is modeled as that of a drift (IMPACT has the capability to track the electrons through the undulator and laser pulse fields, but it is time consuming and unnecessary for our purposes here). The bunch is followed through the LH chicane and a 50-m long collimation section to the entrance of the first Linac section (L1).
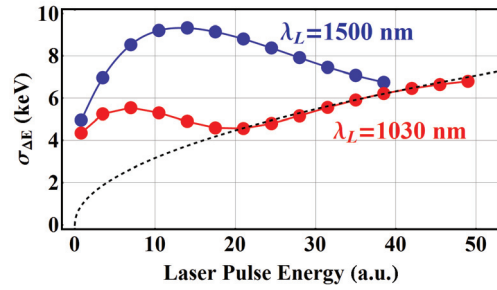
An example of bunchlet longitudinal phase space is shown in Fig. 1, left picture. The prominent energy chirp, entirely due to longitudinal space charge (LSC) in the short bunchlet, is removed in the analysis (linear as well nonlinear terms) before determining the energy spread distribution shown in the right picture. For comparison, the density observed at the exit of the LH chicane (red curve) is also shown: the difference between the two is (mostly) a consequence of the trickle heating effect. The results of a systematic study, shown in Fig. 2, also include data points obtained with λ_L = 1500 nm (blue dots), longer than the design λ_L = 1030 nm (red dots), to illustrate the dependence of trickle heating on the laser wavelength. The black-dashed curve is the nominal rms energy spread $\sigma_{\Delta E} \propto \sqrt{E_L}$ induced by the LH as a function of the laser pulse energy E_L (normalized units). Anomalous heating is apparent for small E_L but remains below the $6-7$ keV LH baseline design specification. The data points follow a behavior qualitatively consistent with the analytical model discussed in [9]. Notice that in the limit of vanishing laser pulse energy, the observed energy spread does not converge to the energy spread of the incoming beam ($\sigma_{E0} \simeq 0.1$ keV, in these simulations), as explained below. The above results are for an earlier and now outdated design of a 4 m long LH chicane with $|R_{56}|$ = 14 mm.

Shot-noise Induced Heating

Another potential source of anomalous heating is the microbunching seeded by shot noise that develops through the LH chicane as a result of energy modulations accrued upstream of the LH. The linear gain of the instability is relatively modest but it may be sufficient for longitudinal space charge in the long section between LH chicane and first magnetic compressor BC1 to cause a few keV amplitude energy-modulation. Strictly speaking, this is a correlated energy spread (with E/z correlations on the μm scale). However, as the beam experiences the relatively large $|R_{56}|$ in BC1 the microcorrelation is flattened causing the energy spread to become effectively uncorrelated. Evidence of enhanced heating is shown on the left picture of Fig. 3 in the (top) data points for the energy spread observed at the entrance of BC1: for low laser-pulse energy, the energy spread is significantly larger than that observed at the entrance of
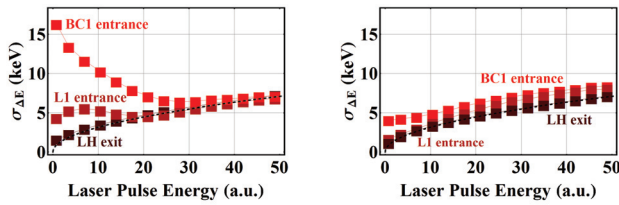
Figure 3: Slice energy spread as observed at the exit of the LH chicane, entrance of L1, and entrance of bunch compressor for a 4 m (left) and improved 8 m long (right; baseline design) LH chicane, showing evidence of shot-noise induced heating; $\sigma_{E0} = 0.1$ keV.

L1 (the latter is for the most part dominated by the trickle heating effect). The data points at the exit of the LH chicane track the nominal heating closely, as expected. The reported energy spread is calculated over a distance within the beam that encompasses several wavelengths of the dominant energy modulation. Once again, this unintended heating is undesirable as it may compromise the ability to tune the LH and set a lower bound to the minimum beam energy spread. The effect is also difficult to predict accurately because of a strong dependence on the not very well-known slice energy spread at the exit of the injector. In addition, there may be contributions to the microbunching instability from the gun and injector, not captured here, also not easy to predict accurately. It is therefore wise to adopt a lattice-design strategy aiming at reducing microbunching amplification through the LH chicane.

The instability is sensitive to the choice of R_{56} in the chicane, a variable over which the lattice designer has some degree of control. All the other relevant parameters kept fixed, there tends to be a value of $|R_{56}|$ that maximizes microbunching. Given the relatively small value of the slice energy spread involved, linear theory shows that here decreasing, rather than increasing, $|R_{56}|$ is the more effective way to reduce the instability. This can be seen from the basic scaling predicted by the simplified linear-theory model of the instability gain for the longitudinal mode with wavenumber k

$$G \simeq 4\pi \frac{I}{\gamma I_A} k |R_{56}| e^{-(\sigma_\delta k R_{56})^2/2} \int ds \frac{|Z(k)|}{Z_0}, \quad (1)$$
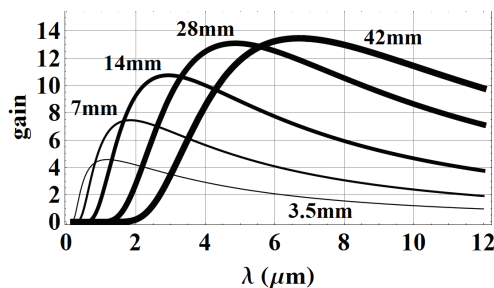
Figure 4: Linear gain curve of the microbunching instability through the LH chicane for several choices of $|R_{56}|$ as indicated. (Constant $\sigma_E = 2.5$ keV through the chicane.)

where I is the bunch peak current, $I_A \simeq 17$ kA the Alfven current, Z the longitudinal space charge impedance per unit length, $Z_0 = 120\pi$ the vacuum impedance and the integral is over the drift space preceding the LH chicane. Several gain curves of the microbunching instability through the LH chicane for various choices of R_{56} are reported in Fig. 4. The model is not very accurate (*e.g.* the beam slice relative energy spread $\sigma_\delta = \sigma_E/E_{inj}$ is assumed to have an effective value constant through the chicane, whereas the generation of the laser-induced heating is localized in the middle of the chicane) but it gives a good sense of the scaling involved. We redesigned the chicane to decrease $|R_{56}|$ to 3.5 mm. In order to keep the trajectory horizontal offset unchanged at 7.5 cm this was achieved by lengthening the chicane to 8 m while reducing the bend angle in the dipoles. Overall, anomalous heating in the presence of the modified chicane is much reduced (right picture in Fig. 3). Both pictures in Fig. 3 were obtained with a conservative choice for the beam natural slice energy spread out of the injector ($\sigma_{E0} = 0.1$ keV).

INSTABILITY THROUGH THE BC'S

It is well known that multi-stage magnetic compression will tend to magnify the development of microbunching [10–12], with the overall instability gain depending on the overlap in frequency domain of the gain curves through each compressor. As the gain through a compressor is sensitive to the details of the beam-slice energy distribution, it is important in the analysis to include the exact form of the energy distribution induced by the laser heater. To illustrate this point let us consider in some detail the development of the instability through BC1 and BC2. Consider the regime in which shot noise is the dominant noise source in the beam exiting the laser heater. As the beam travels toward the first bunch compressor, space-charge induced energy modulations develop and cause bunching as the beam undergoes compression in BC1.

A finite slice energy-spread $\sigma_{\delta,bc1} = \sigma_{E,lh}/E_{bc1}$ introduces a frequency cutoff in the current-profile spectrum of the beam emerging from BC1, suppressing noise amplification at wavelengths shorter than $\lambda_{bc1} \simeq 2\pi|R_{56}^{bc1}|\sigma_{\delta,bc1} \simeq 8.5$ μm (wavelength observed after compression), roughly corresponding to the peak gain, having assumed $\sigma_{E,lh} = 6$ keV heating by the laser heater. (For the other parameters, see Table 1.)

Further LSC-induced energy modulations are then accrued by the beam on its way toward BC2. The spectrum of these modulations exhibiting an expected peak at $\lambda_{bc1}/C_{bc2} \sim 0.85\mu$m is shown in the top-picture of Fig. 5 for a macroparticle beam tracked starting from the exit of the injector with initial water-bag (WB) distribution (*i.e.* a uniformly populated ellipsoid in the 6D phase space). Note that in the figure the spectrum is reported as a function of the wavelength *after* compression through BC2, with $C_{bc2} \simeq 10$. In the simulation we assumed $\sigma_{E0} = 1$ keV for the slice energy spread before passage through the laser heater.
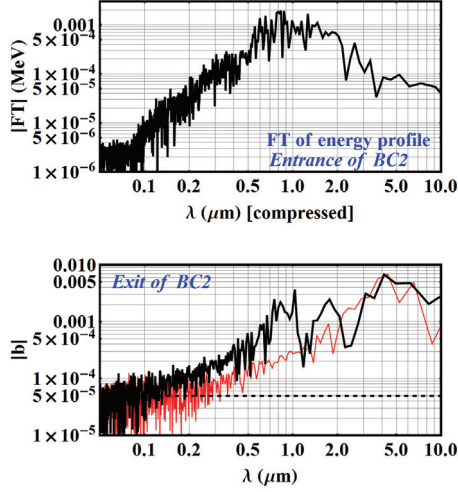
Figure 5: Spectrum of the energy profile of a simulated beam observed at the entrance of BC2 (top) and bunching observed at the exit of BC2 (bottom, black line). In the top picture the spectrum is expressed in terms of mode wavelengths observed after BC2 compression. In the bottom picture the dashed line indicates the shot-noise level; the red line is the bunching exhibited by an equivalent beam with the same $\sigma_E \simeq 36$ keV rms slice energy spread (as observed right before BC2) but with a gaussian slice energy density.

Now, as the slice energy spread after BC1 is $\sigma_{E,bc1} = C_{bc1}\sigma_{E,lh} \simeq 36$ keV we expect bunching to peak at

$$\lambda_{bc2} \simeq 2\pi |R_{56}^{bc2}| \sigma_{\delta,bc2} \simeq 5 \ \mu m \qquad (2)$$

(again, as observed after compression through BC2). Because the spectral components at $\lambda_{bc1}/C_{bc2} \sim 0.85 \ \mu m$ are significantly shorter than λ_{bc2}, the expectation based on a model like (1) is that they should be mostly washed out. In fact, inspection of the spectrum of the beam profile downstream of BC2 shows a strong component in the neighborhood of $\sim 1 \ \mu m$, comparable in magnitude to bunching at $\simeq 5 \ \mu m$, see black curve in the bottom picture of 5. To understand this feature, which leads to interesting consequences further downstream (see next section), we have to account for the effect of the laser heater on the beam energy distribution with more care. (To avoid possible confusion, we should point out that the wavelengths of interest here only coincidentally happen to be in the range of that of the LH laser, $\lambda_L \simeq 1 \mu m$).

Consider a beam model with a sinusoidal energy modulation $\hat{\delta} \sin(k_1 z)$, $k_1 = 2\pi/\lambda_1$ and (uncorrelated) energy density $V(\delta)$. For starters, assume that the beam has no long-scale energy chirp so that no compression occurs. As the beam propagates through a chicane with momentum compaction R_{56} and energy E_{bc}, the beam develops bunching according to

$$\rho(z) = 1 + 2 \sum_{n=1}^{\infty} \tilde{\rho}(k_n) \cos k_n z, \qquad (3)$$
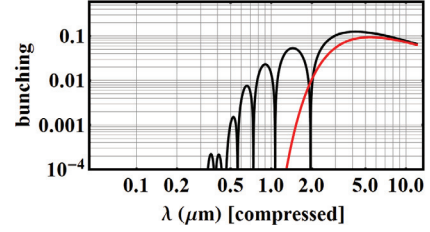
Figure 6: Bunching at the exit of BC2 (black curve) as predicted by Eq. (5) for a model beam with slice energy density as induced by the laser heater and assuming, for simplicity, a uniform spectrum of the energy profile on the beam entering BC2. For comparison, the red curve is the expected bunching from an equivalent beam with identical rms slice energy spread but gaussian distribution, showing a much sharper cut-off at shorter wavelengths. Black and red curve here are meant to capture the essential features of the corresponding curves in the bottom picture of Fig. 5, obtained from macroparticle simulations.

where the FT of the beam density at the exit of the chicane $\tilde{\rho}(k_n) = \lambda_1^{-1} \int_{-\lambda_1/2}^{\lambda_1/2} \rho(z) e^{-ik_n z} dz$ is given by

$$\tilde{\rho}(k_n) = J_n(\hat{\delta} k_1 | R_{56}|) \int d\delta e^{ik_1|R_{56}|\delta} V(\delta). \qquad (4)$$

J_n is the Bessel function and $k_n = nk_1$. This is the generalization of a formula better known when $V(\delta)$ is gaussian [13].

If the laser pulse and the electron beam in the LH are transversally matched one can derive a manageable expression for $V(\delta)$ [14] and evaluate the integral in (4) in terms of a first-order Bessel function

$$\tilde{\rho}(k_n) = J_n(\hat{\delta} k_1 | R_{56}|) \left[\frac{2J_1(x)}{x} \right] e^{-(k_n R_{56}\sigma_{\delta 0})^2/2}, \qquad (5)$$

where $x = \sqrt{2} k_n |R_{56}| \sigma_E/E_{bc}$ and σ_E is the rms energy spread at the entrance of the chicane. With the heater turned off, the beam is assumed to have a gaussian uncorrelated energy distribution with $\sigma_{\delta 0} = \sigma_{E0}/E_{bc}$ rms relative energy spread. In the presence of compression the formulas above are still valid provided that k_n is interpreted as the wavenumber of the beam perturbation as seen *after* compression.

This model applied to the beam dynamics through BC2 is a useful tool for interpreting the simulation results. Plot of Eq. (5) in Fig. 6 for $n = 1$, the only significant component for our parameters, shows that the energy spread induced by the laser heater is associated with a relatively shallow cutoff at shorter wavelengths. Whereas the peak of the gain is not far from the value predicted by Eq. (2), longitudinal modes at shorter wavelength down to 0.5 μm are not strongly suppressed. As a result, modes in the neighborhood of 1 μm after compression in BC1 can pass through BC2 and remain quite visible in the current profile.

Having noted the microbunching amplification in the μm range, we should add that for a LH setting of 6 keV or so, the
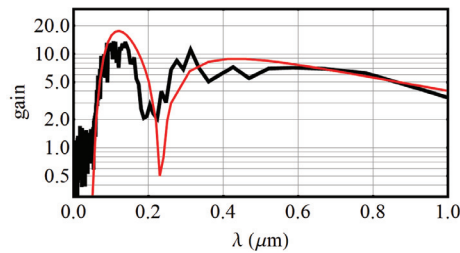
Figure 7: Gain of the instability accrued by the beam traveling from the exit of BC2 through the DL1 dogleg (see text for a description of the machine layout). Linear theory (red curve) agrees fairly well with simulations (black curve). The latter was obtained from a 4-shot average of the bunch profile spectrum.

instability by the exit of BC2 remains modest, amounting to a current ripple of a few percent, see the black curve in Fig. 12. (This curve represents the current profile over a short segment of the same bunch in the example just discussed but observed at the end of the extension line past the Linac). This level of bunching and the concurrent energy spread/modulation would have limited consequences on the FEL performance. However, further amplification of the instability is to be expected as the beam is transported from the Linac to the FELs [15].

TRANSPORT THROUGH THE BYPASS LINE

R_{56} in the Doglegs and its Compensation

The last section of the Linac is followed by an extension line (to accommodate possible future energy upgrades) and a $\sim$ 80 m long, tilted, two-bend dogleg achromat (DL1) designed to gently lift the beam from the floor to the ceiling of the tunnel into the bypass line. Transport past the Linac can add significantly to the instability. A rough, order-of-magnitude estimate of the instability peak gain accrued by the beam from BC2 through DL1, can be done using

$$ G \sim \frac{I}{I_A} \frac{mc^2}{\sigma_E} \frac{L_s}{\gamma^* r_b} \xi \qquad (6) $$

where L_s is the BC2-to-DL1 distance, r_b is an average effective transverse size of the beam and γ^* and effective relativistic factor. This formula is based on the approximation $|Z|/Z_0 \simeq 0.3/\pi\gamma^* r_b$ for the LSC impedance valid when the factor $\xi = 2\pi r_b/\lambda\gamma^*$ is not too far from unity. With a slice energy spread on the order of $\sigma_E = 0.5$ MeV, $I = 850$ A, $L_s = 550$ m, taking for γ^* the geometric mean between the values at BC2 and DL1, and $r_b \simeq 100~\mu$m, we expect a peak gain at about $\lambda \simeq 2\pi(\sigma_E/E_f)|R_{56}| \simeq 0.2~\mu$m, yielding $\xi \sim 0.7$ and hence $G \sim 40$. This is a fairly large number, considering that further amplification is to be expected through the additional transport sections downstream of DL1. It turns out that the above formula overestimates the effect somewhat; however, a more accurate calculation still yields
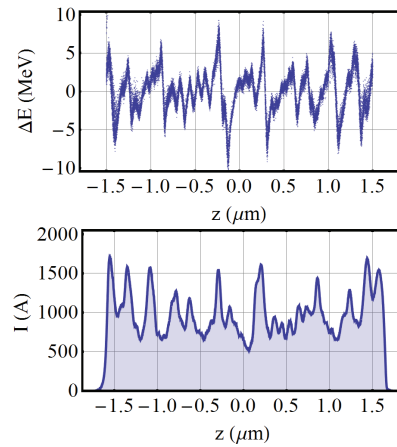
Figure 8: Images of the longitudinal phase space (top) and current profile (bottom) at the entrance of the HXR FEL beamline in the absence of compensating chicanes in the transport line downstream of DL1 show very large instability. (Short flat-top bunchlet with $I = 850$ A current tracked from the exit of BC2).

a significant peak gain $G_{\text{peak}} \sim 15$. This is shown in Fig. 7, where a comparison between the results from linear theory based on an impedance model for space-charge effects (red curve) and macroparticle simulations (black) also provides a reassuring cross-validation of the methods used in our study; in both cases only the longitudinal component of the self-fields is included in the physics model (more on this in the next section). Here, the numerical simulation is for a flat-top beam, with gaussian energy density, propagated from the exit of BC2 and initially carrying no other bunching than that deriving from shot-noise. The black curve is the average of four runs using different seeds in the random number generator employed to populate the macroparticle distribution. The dip observed at about $\lambda \simeq 2~\mu$m is the result of phase differences due to the wavelength-dependent plasma oscillations along the Linac (at these wavelengths the plasma-oscillation period is not very long compared to the distance traveled by the beam; in other words, the kinetic $\propto 1/\gamma^2$ component of R_{56} cannot be neglected, particularly in the vicinity of BC2).

If we now extend the numerical simulation beyond DL1 to the entrance of the FEL we observe a dramatic amplification of the instability, Fig. 8, with maximum seen to occur at the sub-μm wavelength, about consistent with our estimate of the peak gain through DL1. Striking as it is, we should keep in mind that this simulation does not capture the full extend of the instability, as it excludes the beam dynamics upstream of BC2 and bunching that may have occurred therein.

The magnitude of the effect is of serious concern. Fortunately, there exists a simple but effective remedy consisting of introducing R_{56}-compensation in the dispersive sections downstream of the Linac as a way to prevent conversion of modulations in the energy profile into longitudinal slippage (barring the small slippage that may occur as a result of plasma oscillations, which is generally benign).
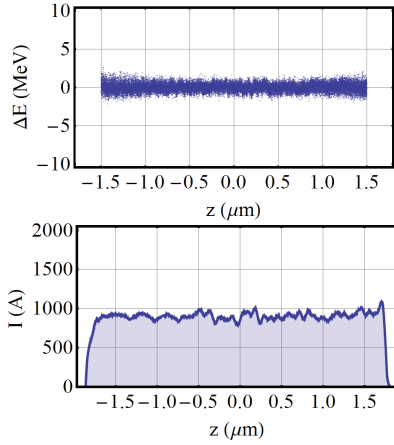
Figure 9: As in Fig. 8 but in the presence of R_{56}-compensating chicanes adjacent to the dipoles of the bypass-line doglegs, showing a much reduced instability.

Figure 10: Longitudinal phase space of the beam core at the entrance of DL1. The red curve is the slice centroid energy. The apparent $\sim 1~\mu$m energy modulation is the result of LSC during acceleration and transport following the second bunch compressor, placed about 700 m upstream of DL1.

Let us consider in some detail the beam transport to the HXR FEL undulator. The main R_{56} contributors to this transport are DL1 ($R_{56} = 200~\mu$m) and a combination of two double-bend achromats downstream of the spreader ($R_{56} = 65 + 65~\mu$m) also arranged in a dogleg configuration. With each dipole in DL1 and downstream dogleg contributing positively to R_{56} a local R_{56}-compensation can be simply achieved by placing standard 4-bend chicanes (contributing negative R_{56}) next to the dogleg dipoles. Because of the small momentum compaction involved, the required compensating chicanes (CCs) are weak and short (~ 1 m). Numerical simulations show a remarkable improvement, Fig. 9, with a similarly beneficial outcome observed in the transport to the SXR FEL.

Exact compensation of the momentum compaction, however, does not completely solve our problems. This becomes apparent when the effect of microbunching accumulated by the beam upstream of, and through BC2, is properly included in the picture, as discussed below.

Effect of Transverse Space-charge Fields

A somewhat surprising finding of our study was the discovery of a new mechanism for the amplification of microbunching occurring in the presence of imperfect damping of the microbunching instability through BC2 and driven by the transverse rather than the longitudinal component of the self-fields. We first observed this effect while investigating the beam dynamics through DL1, including acceleration and transport from the exit of the injector.

Despite the presence of the compensating chicanes we observe a small but significant enhancement of bunching, caused by the transverse space-charge (TSC) forces within the dogleg. The mechanism is somewhat reminiscent of the trickle heating effect [9]: in both cases an energy modulation couples with dispersion to cause the appearance of a 2D longitudinal/horizontal pattern in the beam density on the scale of the energy modulation wavelength at certain locations along the dogleg.
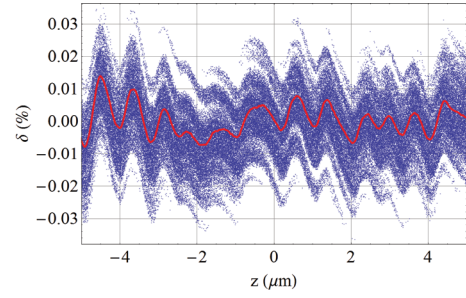
Referring to the WB-beam example discussed earlier, a 6 keV setting of the laser heater leaves a few % microbunching on the beam at $\lambda \simeq 1~\mu$m at the exit of BC2, which by the entrance of the dogleg DL1 results into a noticeable energy modulation, see Fig. 10. Further downstream in the dogleg this modulation gives rise to the pattern seen in Fig. 11. The transverse component of the space charge associated with this 2D x/z pattern causes a μm modulated $\Delta x'$ kick on the particles horizontal angular coordinate. Because the matrix entry R_{52} from location of the kick to exit of the dogleg is generally finite, a longitudinal shift is induced, $\Delta z = R_{52} \Delta x'$, enhancing the existing bunching, as observed at the exit of the dogleg, Fig. 12. The unequivocal 3D nature of the effect is confirmed by simulations where only the longitudinal component of the self-fields is applied in tracking the beam particles. In this case the observed amplification of the observed $\sim 1~\mu$m microbunching disappears.

Under certain simplifying assumptions one can work out an analytical model for the TSC-induced bunching in the form [16]

$$ b_k \simeq \delta_p \frac{2Ik}{\varepsilon_{xn} \gamma^2 I_A} \int_{s_0}^{s_f} ds \frac{\eta_x^2}{\sqrt{\beta_x \beta_y}} e^{-\frac{\varepsilon_{xn} \eta_x^2 k^2}{\gamma \beta_x}}, $$

where δ_p is the relative energy-modulation amplitude at the entrance of the dogleg with wavenumber k, $\beta_{x,y}$ and η_x
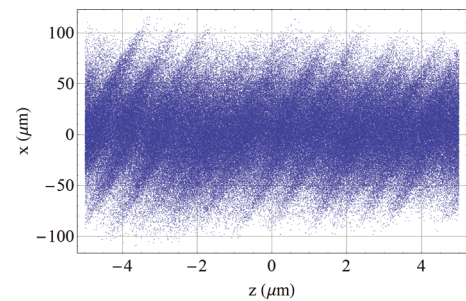
Figure 11: Section x/z of the beam phase space observed just before the first quad of DL1 showing the longitudinal/transverse microbunching induced by the energy modulation of Fig. 10.
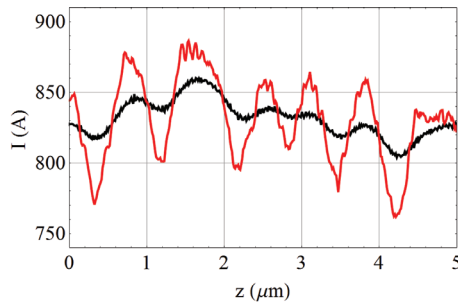
Figure 12: The beam current profile as seen at the entrance of DL1 (black curve) shows ~ 1% longitudinal bunching amplitude at about $\lambda \simeq 1$ μm wavelength. By the exit of the dogleg (red curve) bunching has grown to about 4%, implying a net ~ 3% contribution from TSC in the dogleg. The quoted numbers are about the middle of the observed value ranges.

Figure 13: Bunch longitudinal phase space (top) and current profile (bottom) at the entrance of the HXR FEL. The comparison is between a complete physics-model simulation (right) and one (left) where the linear energy chirp is removed as the beam enters DL1 as a way to highlight the T_{566} effect. (WB beam with $\sigma_E = 6$ keV LH setting. Compensating chicanes are inserted. Bunch head is to the left.)

are the betatron and the dispersion functions, and ε_{xn} is the normalized rms emittance (same as the vertical emittance). The integral is over the dogleg length and the expression is valid for the case where R_{56} has been locally compensated. The formula agrees reasonably well with the results of the numerical simulations and shows that high-brightness beams are most vulnerable to this effect.

The net result of the TSC-induced microbunching from DL1 and the downstream transport sections, including the various other sources of the instability starting from the injector is shown in the right pictures of Fig. 13, for $\sigma_E = 6$ keV LH setting. The observed microbunching is significant. Similar bunching but with somewhat larger magnitude is also observed at the exit of the transport line toward the SXR FEL.

Nonlinear Momentum Compaction

At the entrance of DL1 the bunch carries a significant energy chirp left over from compression and transport through the last section of the Linac and the extension line. Unlike the current LCLS copper machine, the longitudinal wakefields associated with the L-band SC structures are too weak to remove the post-compression chirp. Chirp removal is complete only after transport through the bypass line thanks to the action of the vacuum-chamber resistive-wall wakefields.

It turns out that the $T_{566} \simeq 0.1$ m nonlinear momentum compaction contributed by DL1 in conjunction with substantial energy chirp has the potential to generate further amplification of microbunching. To see this let $\delta_c(z) \simeq hz$ be the energy chirp of the beam at the entrance of DL1, with dominant linear component h. As it travels through the dogleg a particle experiences longitudinal slippage $z' = z + R_{56}\delta + T_{566}\delta^2$.

Consider two particles with approximately the same longitudinal coordinate z_0 but different energy, $\delta_1 = \delta_c(z_0) + \Delta_1$ and $\delta_2 = \delta_c(z_0) + \Delta_2$. Through first order in Δ_1 and Δ_2 the relative slippage between the two reads $\Delta z = R_{56}\Delta\delta + [2T_{566}\delta_c(z_0)]\Delta\delta$, with $\Delta\delta = \Delta_2 - \Delta_1$. In the presence of the

CCs set to exactly cancel the contribution from the doglegs, we have $R_{56} = 0$ and the effect of T_{566} can be thought of as being equivalent to a z-dependent effective $R_{56}^{\text{eff}} = 2T_{566}hz_0$. With $T_{566} \simeq 0.1$ m, $h \simeq 50$ m^{-1}, we have $R_{56}^{\text{eff}} \simeq 100$ μm for $z_0 = 10$ μm away from the beam center, *i.e.* a value comparable in magnitude to the actual linear momentum compaction of the DL1 dogleg in the absence of the compensating chicanes. The simplest way to gauge the T_{566}-effect is by a macroparticle simulation in which 'by hand' we remove the beam linear energy chirp right at the entrance of DL1 and compare the result (left pictures in Fig. 13) with that of the baseline simulation (same figure, right pictures, where the T_{566} effect is included). The T_{566} effect is particularly visible toward the tail of the bunch; in other parts of the beam the behavior is more complicated as it appears to interfere with other sources of the instability. Incidentally, we should note that, for better comparison, in the simulation the resistive wall wakefields were turned off in order to preserve the longitudinal phase-space flatness of the beam delivered to the FEL.

CONCLUSIONS

To summarize our main findings, we have determined that *i)* transport through the bypass and distribution lines downstream of the Linac can significantly amplify the microbunching instability and *ii)* the instability is fueled by two distinct sources: longitudinal and transverse space charge. We showed that introducing local R_{56} compensation in the transport lines downstream of the Linac has a beneficial effect but still leaves a sizeable level of instability when the laser heater is operated at its design specification.

Is there a way, short of heating the beam more, to reduce the instability further? We recognize that setting the compensating chicanes to cancel R_{56} minimizes the LSC-induced microbunching. However, in view of *ii)* it is conceivable that LSC- and TSC-induced bunching could, to some de-
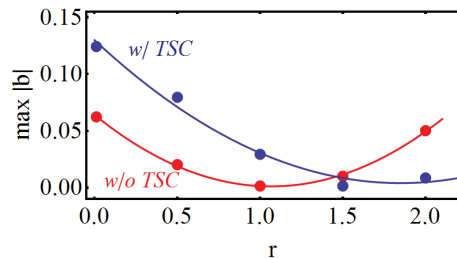
Figure 14: Amplitude of the instability observed on the beam at the entrance of the HXR FEL as a function of the strength of the compensating chicanes with (blue data) and without (red data) inclusion of transverse space-charge effects in the simulation. See the text for the meaning of r. Water-bag beam with 6 keV LH setting. The simulations do not include the T_{566}-effect.

Figure 15: Energy spread observed on the beam at the entrance of the HXR FEL as a function of the LH setting for two lattice designs: with exact compensation ($r = 1$, blue data) and over-compensation ($r = 1.5$, red data) of R_{56} in the bypass doglegs. The simulations include the T_{566}-effect.

gree, offset each other, suggesting that a different tuning of the compensating chicanes may yield an improved lattice. Indeed, simulations starting from the injector show minimum bunching when the CCs overcompensate rather than exactly cancel the R_{56} contribution from the adjacent dogleg dipoles.

Fig. 14 reports a measure of the instability at the FEL as a function of the parameter r defined as $r = |R_{56}^{CC}|/|R_{56}^{B-DL}|$, where R_{56}^{B-DL} and R_{56}^{CC} are the contributions to the momentum compaction from the dipole(s) in the dogleg and the associated CC; $r = 1$ corresponds to exact compensation as in the simulations of Fig.'s 9 and 13. The measure of the instability in Fig. 14 is the maximum bunching $|b(k)|$ for $\lambda = 2\pi/k \leq 3\ \mu m$ obtained from the FT of the current profile in the bunch core. While $r = 1$ represents the optimum in simulations where we exclude account of the transverse component of space-charge fields on the beam dynamics (red dots), with the full 3D model of space charge the minimum instability shifts to about $r \simeq 1.5$ (blue dots). To facilitate the interpretation of the results, in these simulations we removed the linear energy chirp from the beam at the entrance of DL1 as a way to eliminate the T_{566} effect. Including the latter, however, does not alter the results significantly.

To further validate these conclusions, we studied the dependence of the beam energy spread at the FEL (an alternate measure of the microbunching instability more directly related to the FEL performance) as a function of the LH setting for $r = 1$ and $r = 1.5$, see Fig. 15. The dashed line represents the expected energy spread in the absence of collective effects $\sigma_E = C\sigma_{E,lh}$, where C is the overall magnetic compression. In the data analysis, σ_E is calculated as the projected rms energy spread within the $\sim 20\ \mu m$ long beam core after we remove the long-scale nonlinear energy chirp from the beam distribution as determined by a low-order polynomial interpolation (therefore, properly speaking, σ_E is not a *slice* energy spread). The simulations include the T_{566} effect and indicate a minimum achievable energy spread, as defined above, of 0.65 MeV corresponding to laser heater settings of about 9 keV.
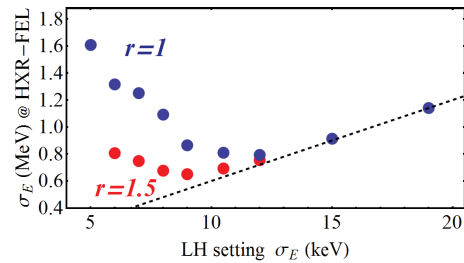
Additional machine optimization to reduce the instability further may be possible in principle targeting, for example, the reduction of the $\sim 1\ \mu m$ bunching observed at the exit of BC2. This could be pursued, *e.g.*, by retuning the bunch compressor chicanes R_{56} to minimize the overlap of the instability gain curves through each compressor. In practice, other constraints limit the freedom to set the BC parameters and the payoff from further lattice optimization is likely to be modest. On the other hand, we believe that the current baseline lattice with the compensating chicanes properly tuned should already deliver beams meeting the desired FEL performance in both the SASE and self-seeding modes of operation.

ACKNOWLEDGMENTS

REFERENCES

[1] J. Galayda, IPAC 2014, Dresden, Proc., p. 935 (2014).

[2] T. Raubenheimer, 'LCLS-II: Status of the CW X-ray FEL Upgrade to the SLAC LCLS facility', Proc. 37th Int. Free-Electron Laser Conf., Daejeon (2015).

[3] C. Limborg-Deprey, P. Emma, Z. Huang, and J. Wu, EPAC 2004, Lucerne, Proc. p. 1506 (2004).

[4] M. Venturini, *et al.*, PRST-AB, **13**, 080703 (2010).

[5] J. Qiang, J. Corlett, C.E. Mitchell, C.F. Papadopoulos, G. Penn, M. Placidi, M. Reinsch, R.D. Ryne, F. Sannibale, C. Sun, M. Venturini, P. Emma, and S. Reiche, PRST-AB, **17**, 030701 (2014).

[6] J. Qiang, *et al.*, PRST-AB **12**, 100702 (2009).

[7] J. Qiang, *et al.* 'Start-to-end simulation of the LCLS-II beam delivery system with real number of electrons', Proc. 37th Int. Free-Electron Laser Conf., Daejeon (2015).

[8] G. Marcus, *et al.*, 'High-fidelity start-to-end numerical particle simulations and performance studies for LCLS-II', Proc. 37th Int. Free-Electron Laser Conf., Daejeon (2015).

[9] Z. Huang, *et al.*, PRST-AB **11**, 020703 (2010).

[10] M. Venturini, PRST-AB **7**, 104401 (2007).

[11] E.A. Schneidmiller and M.V. Yurkov, PRST-AB **13**, 110701 (2010).

[12] A. Marinelli, *et al.* , PRL **110**, 26480-2 (2013).

[13] L. H. Yu, Phys. Rev. A **44**, 5178 (1991).

[14] Z. Huang, M. Borland, P. Emma, J. Wu, C. Limborg, G. Stupakov, and J. Welch, PRST-AB **7**, 074401 (2004).

[15] M. Venturini and A. Zholents, NIM-A **539**, 53 (2008).

[16] M. Venturini and J. Qiang, PRST-AB **18**, 054401 (2015).